SIAM J. APPL. MATH.
Vol. 68, No. 1, pp. 239–252

STATISTICAL RECONSTRUCTION OF VELOCITY PROFILES FOR NANOPARTICLE IMAGE VELOCIMETRY*

CHRISTEL HOHENEGGER† AND PETER J. MUCHA‡

Abstract. Velocities and Brownian effects at nanoscales near channel walls can be measured experimentally in an image plane parallel to the wall by evanescent wave illumination techniques [R. Sadr, M. Yoda, Z. Zheng, and A. T. Conlisk, *J. Fluid Mech.*, 506 (2004), pp. 357–367], but the depth of field in this technique is difficult to modify. Assuming mobility of spherical particles dominated by hydrodynamic interaction between particle and wall, the out-of-plane dependence of the mobility and in-plane velocity are clearly coupled. We investigate such systems computationally, using a Milstein algorithm that is both weak- and strong-order 1. In particle image velocimetry (PIV), image pairs are cross-correlated to approximate the mean displacement of n matched particles between two windows. For comparison, we demonstrate that a maximum likelihood algorithm can reconstruct the out-of-plane velocity profile, as specified velocities at multiple points, given known mobility dependence and perfect mean measurements. We then test this reconstruction for noisy measurements as might be encountered in experimental data. Physical parameters are chosen to be as close as possible to the experimental parameters while we consider three types of velocity profiles (linear, parabolic, and exponentially decaying).

Key words. stochastic differential equations, maximum likelihood estimate, particle image velocimetry, velocity profile, wall effects

AMS subject classifications. 76M35, 76M25, 76D99, 60G99, 65C35

DOI. 10.1137/050648043

1. Introduction.

Fluid velocities in a channel can be measured by illumination and imaging of tracer particles under the assumption that they follow the flow, with corrections possibly applied for effects including, e.g., the near-wall relationship between particle translation and rotation [6]. For laser-Doppler velocimetry, Fuller et al. [3] showed that it is possible to reconstruct the velocity gradient in a laminar flow using light-scattering spectroscopy. This requires the knowledge of the intensity function and the technical capacity of turning the sample to get a proper angle of illumination. At microscales, Meinhart et al. (see [15], [11], [10]) developed an illumination technique, particle image velocimetry (PIV), to replace spectroscopy, where the tracers are illuminated using multiple laser sheets and the velocity profile is computed as means over successive windows using cross-correlation techniques. Again the sample has to be properly illuminated so that particles remain in the focal plane. If it is possible to turn the sample, all components of the mean velocity profile can be obtained.

At nanoscales, including the near-wall region of microchannels, Sadr, Li, and Yoda [12] and Sadr et al. [14] extend PIV to flows illuminated with evanescent waves generated by total internal reflection at the wall. Image pairs are captured on a cam-

*Received by the editors December 20, 2005; accepted for publication (in revised form) June 18, 2007; published electronically October 24, 2007. This work was partially supported by the Department of Energy (DE-FG-02-03ER25567), the National Science Foundation (DMS-0204309), and start-up funds provided by the Institute for Advanced Materials and the Department of Mathematics at the University of North Carolina at Chapel Hill.

http://www.siam.org/journals/siap/68-1/64804.html

†Courant Institute of Mathematical Sciences, University of New York, New York, NY 10012 (choheneg@cims.nyu.edu).

‡Department of Mathematics & Institute for Advanced Materials, University of North Carolina, Chapel Hill, NC 27599 (mucha@unc.edu).

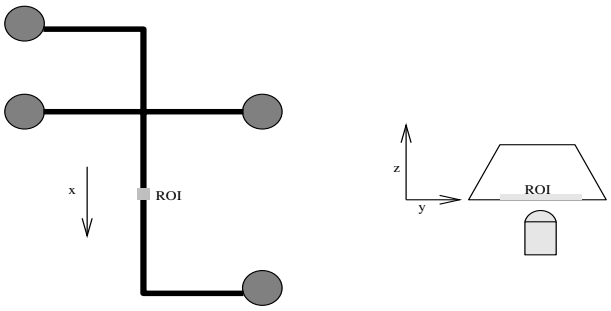

FIG. 1.1. *Experimental setup: Region of interest, flow direction, and wall location.*

era with a time interval $\sim$ 2ms, and in-image-plane mean velocities are obtained using cross-correlation techniques. Figure 1.1 illustrates the experimental setup around the region of interest and some of the inherent experimental restrictions. While Sadr, Li, and Yoda [12] show that Brownian diffusion can cause additional errors in the measurements as particles drop in and out of the imaged window, only limited information about the velocity along or dependence on the out-of-plane coordinate has been experimentally accessed recently from the brightness of the images and the decay of the illumination function [6], [7], [9]. Questions remain about the accuracy and range of validity of processing based on image intensity, especially in the presence of the highly heterogeneous distribution of fluorescent dye on the tracer particle surfaces, while background noise pollutes the images causing reconstruction of velocity profile based solely on intensity to be extremely challenging (see Li, Sadr, and Yoda [9]).

Another dominant difficulty of these measurements arises from the nonconstant diffusion tensor induced by the proximity of the wall. Both the in-plane and out-of-plane diffusion components strongly depend on the distance from the wall (see Figure 2.1(a)). While this dependence is well understood in terms of the hydrodynamic interaction between particle and wall [1], the effect of such diffusion on the resulting measurements has been only recently addressed experimentally (see, e.g., [14]). Meanwhile, significant effort has been put into extending the range of validity of particle image velocimetry (PIV) and particle tracking velocimetry (PTV) to smaller ranges of particles. For example, Guasto, Huang, and Breuer [4] use a statistical approach assuming nearly constant diffusion to eliminate experimental noise (drop-in/-out, mismatch, particles blinking) and obtain a distribution of velocities. Using a similar idea with nonconstant diffusion, Jin et al. (see [6], [7]) notice in their attempts to assess slip at the wall that a nonnegligible difference exists between the apparent measured mean velocities and the imposed shear rate. Interpretations of such studies are further complicated by the measured velocities representing those across a spatially extended region away from the wall, typically with little mechanism for modifying the extent of such a region.

In this work, we show that it is possible to reconstruct the out-of-plane dependence of the in-plane velocity component as a collection of velocities at specified out-of-plane distances (typically five points), based solely on in-plane images. The unique assumption leading to the statistical reconstruction of the out-of-plane component concerns the out-of-plane distribution of the particles between two window measurements. For simplicity, here we assume that the computational and observational domains are the same, thereby eliminating errors due to particle drop-in/-out for this proof-of-principle demonstration.

The next two sections present the particle model incorporating the most important parameters from the experiments and its numerical simulation with a strong order 1 scheme. In the fourth section we develop the algorithm for the perfect case, in which the mean displacements are known exactly. The reconstruction is illustrated for three different specified velocity test profiles (see Figure 2.1(b)): a linear profile, a parabolic profile, and a profile exponentially decaying to the bulk velocity. In the fifth section we extend the idea to noisy mean displacements obtained through the consideration of a measurement error similar to the one reported for cross-correlation from simulated images (PIV techniques). Finally, we discuss the limitations of the model and its possible improvement.

2. Particle model. We test the algorithmic reconstruction on a simple stochastic model of particle motion. Each particle is assumed to have a fixed radius a ($a = 50\,\mathrm{nm}$ in the demonstrations here), and the hydrodynamic interaction between the wall and a particle is captured by the model for mobility in terms of the out-of-plane coordinate perpendicular to the wall, z. We ignore particle-particle hydrodynamic interactions, which are relatively small for the dilute particle volume fractions of the experiments. The tracer particles are dragged along with the fluid flow; additional interactions between particles and the wall are feasible but not included here.

We consider a system of n ($n = 64$) Brownian particles obeying Stokes drag relations, linearly dependent on the velocity. For time steps Δt bigger than the force relaxation time, Ermak and McCammon [2] show that the displacement Δr_i can be expressed as

$$\Delta r_i = \sum_{j=1}^{3n} \frac{\partial D_{ij}}{\partial r_j}\Delta t + \sum_{j=1}^{3n} \frac{D_{ij}F_j}{k\Theta}\Delta t + W_i(\Delta t), \quad i = 1, \ldots, 3n, \tag{2.1}$$

where $W_i(\Delta t)$ is a random displacement with a Gaussian distribution function whose average value is zero and whose variance-covariance matrix is $2\mathbf{D}\Delta t$, $\mathbf{D}$ is the diffusion tensor, $\mathbf{F}$ are the external forces, k is the Boltzmann constant, and Θ is the temperature. The Brownian displacement can be expressed as [2]

$$W_i(\Delta t) = \sum_{j=1}^{i} \sigma_{ij} dW_j, \quad \sigma = \sqrt{\mathbf{2D}}, \quad dW_j = \mathcal{N}(0, \Delta t), \quad j = 1, \ldots, 3n, \tag{2.2}$$

where $\mathcal{N}(\mu, \sigma^2)$ indicates Gaussian random variables of mean μ and variance σ^2.

While we ignore particle-particle interactions, hindered Brownian diffusion due to hydrodynamic particle-wall interactions is an important effect for the near-wall conditions in the experiments. A first approximation of the nonconstant diffusion tensor is obtained by the methods of image singularities for Stokes flows, valid for particle center-to-wall distances, z, that are large compared to the particle radius, a. For our model system here, we include for simplicity only the lowest-order a/z corrections for diffusion components parallel to the planar wall but instead employ the Bevan–Prieve relation [1] for the out-of-plane diffusion perpendicular to the wall, both because of its experimental verification and because it includes the physically impermeable property that the diffusion coefficient goes to zero for a spherical particle touching the wall ($z = a$):

$$\mathbf{D} = \frac{k\Theta}{6\pi\mu a} \begin{pmatrix} 1 - \frac{9}{16}\frac{a}{z} & 0 & 0 \\ 0 & 1 - \frac{9}{16}\frac{a}{z} & 0 \\ 0 & 0 & \frac{6z^2 - 10az + 4a^2}{6z^2 - 3az - a^2} \end{pmatrix} = D_\infty \beta(z), \tag{2.3}$$

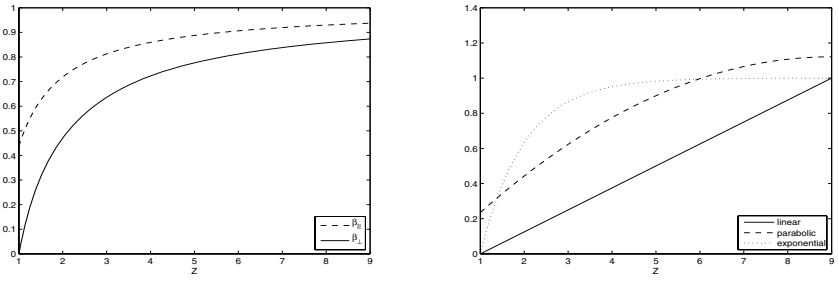

(a) Components of $\beta(\frac{z}{a})$ (b) Velocity profiles $\gamma(\frac{z}{a})$

FIG. 2.1. (a) *Dimensionless diffusion coefficients perpendicular $\beta_\perp$ and parallel $\beta_{||}$ to the wall.* (b) *Dimensionless velocity profiles γ for the linear, parabolic, and exponentially decaying test cases.*

for the three components of each individual particle, where $D_\infty = k\Theta/(6\pi\mu a)$ is the Stokes–Einstein relation in the bulk limit far from the wall, the z-component is along the direction perpendicular to the wall, and z is the distance between the center of the particle and the wall.

Here we consider a simulated channel of height H with three different test flows $u_\infty\gamma(z)\mathbf{e_x}$ with "bulk velocity" u_∞, as might be encountered in shear flow, pressure-driven flow, and electroosmotically pumped flow, respectively: linear flow $\gamma(z) = \frac{1}{H-a}(z-a)$, parabolic flow $\gamma(z) = \frac{4}{(2H-a)^2}z(2H-z)$, and an exponentially decaying profile $\gamma(z) = 1 - \exp(1 - z/a)$ (Figure 2.1(b)). For simplicity, we consider the above flows to be the force-free velocity profiles of the tracer particles themselves, with the hydrodynamic balance given for the external forces on the particles $\mathbf{F} = k\Theta\mathbf{D}^{-1}u_\infty\gamma(z)\mathbf{e_x}$. In the physical experiments, additional corrections are required to relate the force-free velocities of the tracers to those of the underlying flow (see, e.g., [6]); we assume such corrections can be imposed if the particle velocities are accurately measured, proceeding with simulations of imposed particle velocities whose velocity profiles we will reconstruct. Here we include only flow along one (x) of the two in-plane directions parallel to the wall, but since the statistical reconstructions below will not process any displacements along the other in-plane direction (y), the methods presented here can be equivalently applied to measure any in-plane flow profile dependent on the out-of-plane (z-) direction.

Our model stochastic ODE Langevin equation for the displacement of an individual particle is then

$$dx = u_\infty\gamma(z)\,dt + \sqrt{2D_\infty\beta_{||}(z)}\,dW_1, \tag{2.4}$$

$$dy = \sqrt{2D_\infty\beta_{||}(z)}\,dW_2, \tag{2.5}$$

$$dz = D_\infty\frac{d\beta_\perp(z)}{dz}\,dt + \sqrt{2D_\infty\beta_\perp(z)}\,dW_3. \tag{2.6}$$

Letting T be the time elapsed between two PIV-window observed images, we set T and the radius a as the characteristic time and length scales, respectively. Letting $x = aX$, $y = aY$, $z = aZ$, and $t = T\tau$ define the dimensionless variables, the resulting dimensionless parameters are $\Pi_1 = \frac{u_\infty T}{a}$ and $\Pi_2 = \frac{D_\infty T}{a^2}$. For our tests reported here, we select $T = 2^{-9}$s, giving $\Pi_2 = 4$ at $\Theta = 300$, with u_∞ selected to give $\Pi_1 = 3$, of

a scale typical to those of the experiments. Our dimensionless Langevin model, with $d\mathbf{W} = \mathcal{N}(0, d\tau)$, becomes

$$dX = \Pi_1 \gamma(aZ)\, d\tau + \sqrt{2\Pi_2 \beta_{||}(aZ)} dW_X, \tag{2.7}$$

$$dY = \sqrt{2\Pi_2 \beta_{||}(aZ)}\, dW_Y, \tag{2.8}$$

$$dZ = \Pi_2 \frac{d\beta_\perp(aZ)}{dZ}\, d\tau + \sqrt{2\Pi_2 \beta_\perp(aZ)}\, dW_Z. \tag{2.9}$$

3. Numerical simulation. Equations (2.7), (2.8), and (2.9) form a system of stochastic differential equations of the form $d\mathbf{X} = \mathbf{f}(\mathbf{X}, t)d\tau + \mathbf{g}(\mathbf{X}, t)d\mathbf{W}$. We solve it with a Milstein scheme of weak and strong order of convergence one. The coupling of the system through the Z-component yields a nondiagonal noise in the stochastic differential equation sense. The resulting Milstein scheme is given by [8] (see also [5]):

$$X_{j+1} = X_j + f_{1,j}\Delta\tau + g_{11,j}\Delta W_{1,j} + \frac{1}{2} g_{11,j} \left.\frac{dg_{11}(z)}{dZ}\right|_{Z=Z_j} I_{(3,1)}, \tag{3.1}$$

$$Y_{j+1} = Y_j + f_{2,j}\Delta\tau + g_{22,j}\Delta W_{2,j} + \frac{1}{2} g_{22,j} \left.\frac{dg_{22}(Z)}{dZ}\right|_{Z=Z_j} I_{(3,2)}, \tag{3.2}$$

$$Z_{j+1} = Z_j + f_{3,j}\Delta\tau + g_{33,j}\Delta W_{3,j} + \frac{1}{2} g_{33,j} \left.\frac{dg_{33}(Z)}{dZ}\right|_{Z=Z_j} \Big((\Delta W_{3,j})^2 - \Delta\tau\Big), \tag{3.3}$$

where $f_{i,j} = f_i(Z_j)$, $g_{ii,j} = g_{ii}(Z_j)$, and $I_{(3,i)}$ $(i = 1, 2)$ are the double Itô stochastic integrals defined as $I_{(3,i)} = \int_{t_k}^{t_{k+1}} \int_{t_k}^{t_{k+1}} dW_3 dW_i$. Since $I_{(3,i)}$ has no closed analytical solution, we approximate $I_{(3,i)}$ as the solution of a stochastic differential system:

$$I_{(3,i)} = X_i(t_{k+1}), \quad \text{where} \quad \begin{cases} dX_i = X_3 dW_i, & X_i(t_k) = 0, \\ dX_3 = dW_3, & X_3(t_k) = 0. \end{cases} \tag{3.4}$$

Equation (3.4) is solved using Euler–Maruyama steps, the stochastic equivalent of a forward Euler step, with strong order of convergence $\frac{1}{2}$. To ensure convergence to an accurate solution for the entire system, we choose $\Delta\tau = 2^{-10}$ in (3.1)–(3.3), resolving each Itô integral $I_{(3,i)}$ with 2^{10} time steps in (3.4).

4. Reconstruction with perfect means. We start our proof-of-principle calculations by statistically reconstructing velocity profiles based on perfectly observed mean displacements. By this we mean that the true position of each particle is known and the mean displacement of the n particles between two image-pair windows is computed exactly. Cross-correlation processing of image pairs in PIV extracts, up to various sources of error, the mean displacement of the "matched" particles—those that contribute to both images. If the true displacement of each particle could be experimentally determined, as in particle tracking, then the same reconstruction ideas below do apply, but our various tests indicated that such particle tracking does not improve the results, and may even require greater quantities of data than statistical reconstruction based on mean displacements, presumably because of the statistical reliance below on clearly characterized Brownian displacements.

Let $f_{\Delta X}$ be the probability distribution function of a displacement ΔX. From (2.7) the X-displacement depends on the Z-position. Therefore we define $f_{\Delta X|Z}$ to

be the probability density function of ΔX given Z. Then

$$f_{\Delta X} = \int f_{\Delta X|Z} f_Z dZ, \tag{4.1}$$

where f_Z is the probability density function of particles in Z. Because we restrict ourselves to the case where the computation and observation domain are the same, we make the following assumption about the Z distribution:

$$f_Z = \frac{a}{H-a}\chi_{[1,H/a]}, \tag{4.2}$$

where χ_I is the characteristic function on an interval I.

Next we make a fundamental simplifying modeling assumption for the reconstruction: that the particle displacements over the time T between two consecutive windows can be approximated by an Euler step of the form

$$\Delta X \approx \Pi_1\gamma(aZ) + \sqrt{2\Pi_2\beta_{||}(aZ)}dW \quad \text{with } dW = \mathcal{N}(0,1), \tag{4.3}$$

where $\gamma(aZ)$ is the unknown velocity profile. From (4.3) we conclude that

$$f_{\Delta X|Z} = \frac{1}{2\sqrt{\pi\Pi_2\beta_{||}(aZ)}} e^{-\frac{(\Delta X - \Pi_1\gamma(aZ))^2}{4\Pi_2\beta_{||}(aZ)}}. \tag{4.4}$$

Finally, using (4.1), (4.2), and (4.4) we find that

$$f_{\Delta X} = \frac{a}{2\sqrt{\pi\Pi_2}(H-a)} \int_1^{\frac{H}{a}} \frac{1}{\sqrt{\beta_{||}(aZ)}} e^{-\frac{(\Delta X - \Pi_1\gamma(aZ))^2}{4\Pi_2\beta_{||}(aZ)}} dZ. \tag{4.5}$$

Let $\overline{\Delta X}$ be the mean displacement of n matched particles over a window and let f_S be the probability density function of $n\overline{\Delta X}$. Now let f be the joint probability density function of N measured $n\overline{\Delta X}$. A standard result of probability, together with the assumption of independence between two windows measurement, yields

$$f_S = f_{\Delta X} * \cdots * f_{\Delta X} \quad \text{and} \quad f = \prod_{i=1}^{N} f_S, \tag{4.6}$$

where $*$ denotes the convolution. This independence assumption is, of course, incorrect, since consecutive $\overline{\Delta X}$ displacements are correlated by the continuity-in-time of the particles z positions; we nevertheless proceed under this modeling assumption, counting on the effect of the correlations to be sufficiently small.

Figure 4.1 compares the histogram of a $n\overline{\Delta X}$ data set with $Z \in [1, H/a]$ for the parabolic test profile with the probability density function obtained with (4.5) (dashed line). The integral in (4.5) is computed with a Gauss–Legendre quadrature formula under the assumption of a uniform z-distribution. This demonstrates the reasonable validity of assumption (4.3). Going even further, the dotted line in Figure 4.1 represents the probability density function obtained by fitting the data set $n\overline{\Delta X}$ for $Z \in [1, H/a]$ by a single Gaussian. The differences between the integrated Gaussian (dashed line) and the fitted Gaussian (dotted line) are minimal in the height and location of the peak. These minimal distinctions make the desired optimization highly sensitive. Despite these expected difficulties, we nevertheless continue both with our assumption (4.3) and the fundamental ideas of the velocity profile reconstruction.

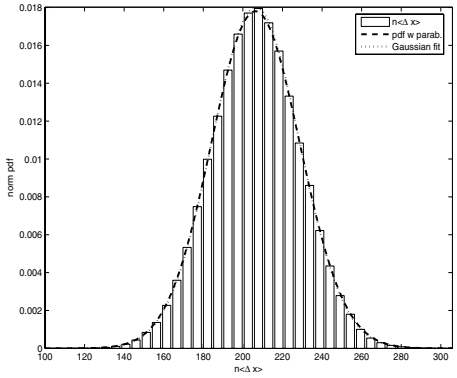

FIG. 4.1. *Comparison of the parabolic profile between the histogram of the distribution of* $n\overline{\Delta X}$*, the probability density function* (4.5)*, and a fitted Gaussian.*

Given N measured mean values $n\overline{\Delta X}$, Π_1, Π_2, and $\beta_{||}(aZ)$, the maximum likelihood estimate of $\gamma(aZ)$ is the value of $\gamma(aZ)$ that makes the observed means most likely. Led by the independence assumption, we define the log-likelihood function

$$\phi(\{\gamma_j\}_{j=1}^{M}) = -\ln f \overset{(4.6)}{=} -\sum_{i=1}^{N} \ln f_S(n\overline{\Delta X}), \tag{4.7}$$

where M is the number of discrete points Z at which we estimate γ. The most likely values for γ_j, $j = 1, \ldots, M$, are obtained by minimizing the log-likelihood function ϕ (4.7) of the M variables $\gamma_1, \ldots, \gamma_M$ for a data set $n\overline{\Delta X}$ of size N.

The statistical reconstruction problem has thus been reduced to two numerical algorithms. First, we evaluate the probability density function f_S in (4.6) by repeated convolution of the probability density function $f_{\Delta X}$ as in (4.5), computing the integral by Gauss–Legendre quadrature for given γ_j values at the Legendre collocation points $Z_j \in [1, H/a]$ for $j = 1, \ldots, M$. We subsequently minimize the function ϕ (4.7) with a direct simplex algorithm penalizing solutions that do not produce an increasing sequence, since we know that the velocity profile is increasing to the bulk velocity away from the wall. We also experimented with the alternative scheme of minimizing ϕ over low-order polynomials for $\gamma(aZ)$ but did not obtain results any more promising than those presented below. Not surprisingly, the minimization routine is highly sensitive to the choice of the initial guess. Therefore, when reconstructing velocity values for a small number of points M, we first search the M-dimensional space for a suitable initial guess by evaluating the function at a fixed number of increasing grid points. When reconstructing velocity values at M points for M larger (say, $M \geq 7$), we interpolate the initial guess from the reconstructed velocity values for smaller M.

Figure 4.2 illustrates the reconstruction for the linear and parabolic profiles at five points ($M = 5$) for two different data sizes. Since the accuracy of the reconstructed points does not appear to improve when N increases from 2^{14} to 2^{18}, we are motivated to instead consider breaking one block of data up into separate reconstructions over each of B blocks of size 2^b. Figure 4.3 contains semilog plots of the L^2 relative error of the reconstructed γ_j, $j = 1, \ldots, M$, with respect to the true $\gamma(aZ_j)$, $j = 1, \ldots, M$, for individual blocks, the errors averaged over the number of blocks B for four different values of M (3, 5, 7, and 9 points). For the linear profile on the left, we observe the same behavior as in Figure 4.2, namely, that increasing the data size does not

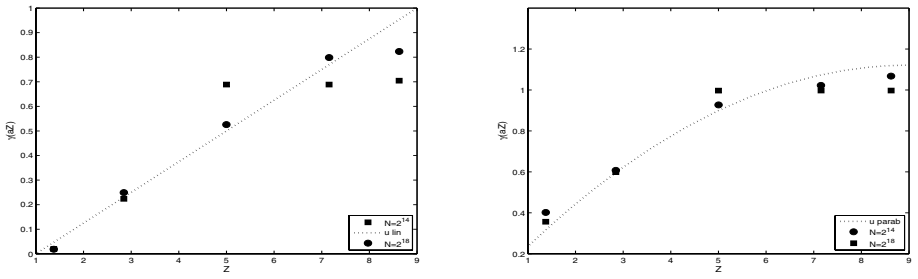

(a) Linear profile (b) Parabolic profile

FIG. 4.2. *Velocity profile reconstruction at $M = 5$ points for the linear and parabolic test profiles with data set sizes $N = 2^{14}$ and $N = 2^{18}$.*

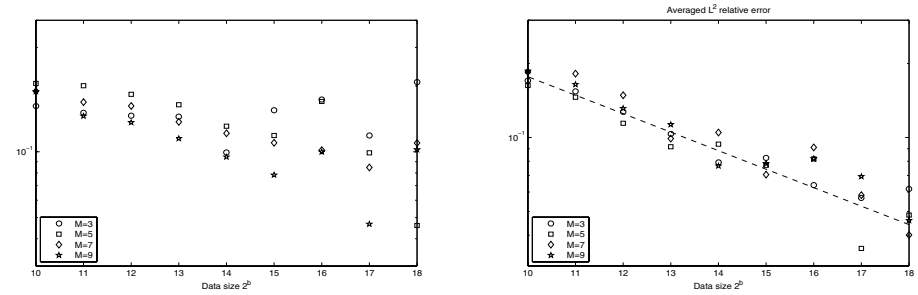

(a) Linear profile (b) Parabolic profile

FIG. 4.3. *L^2 relative error averaged over the number of blocks B of size 2^b at $M = 3$, $M = 5$, $M = 7$, $M = 9$.*

predictably improve the accuracy of the reconstruction after some point. For the parabolic profile on the right, we find a decay of the relative error in the function of the data size b which appears to be roughly $(2^b)^{-1/4}$ up to another apparent stagnation of the decaying error for data sizes larger than 2^{14} or 2^{15}. We next consider the plot of the L^2-norm of the relative error of the block-averaged reconstructed values $\overline{\gamma_j} = \frac{1}{B}\sum_{k=1}^{B} \gamma_j^k$, $j = 1, \ldots, M$ (where γ_j^k is the reconstructed value at Z_j for the block B_k), with respect to the true $\gamma(aZ_j)$, $j = 1, \ldots, M$ (Figure 4.4). We deduce from the relative errors of the block-averaged values, especially for the parabolic test profile, that errors can be reduced by such averaging over a limited number of blocks. As above, the parabolic profile follows a decay close to $(2^b)^{-1/4}$ up to 2^{15}. We do not at present have any explanation for this particular power law of decay. We conclude that the best reconstruction on a data set of the size $N = 2^{18}$ will be achieved when the average of the reconstructed profile is done over 8 or 16 blocks. We also notice that increasing the number of discrete points to $M = 7$ or $M = 9$ does not produce significantly different normed errors but provides more detail about the calculated profile at the cost of a lengthier computation.

In practice, of course, the goal of the reconstruction is to obtain an approximation of the velocity profile, the true profile being unknown. So, finally, we compare the L^1-norm of the variance of the reconstructed profiles from the individual blocks, plotted

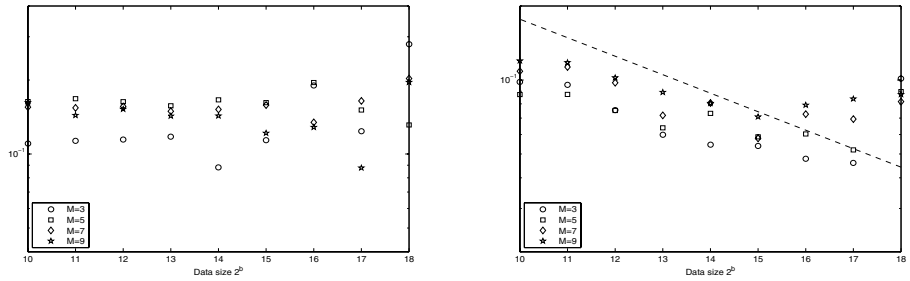

(a) Linear profile (b) Parabolic profile

FIG. 4.4. *L^2 relative error with γ averaged over the number of blocks B of size 2^b at $M = 3$, $M = 5$, $M = 7$, $M = 9$.*

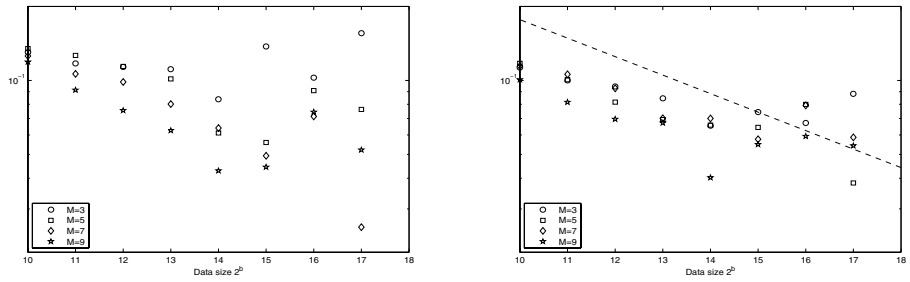

(a) Linear profile (b) Parabolic profile

FIG. 4.5. *L^1-norm of the variance of γ averaged over the number of blocks B at $M = 3, 5, 7, 9$ for the linear and parabolic profile.*

versus the exponent b in the block size 2^b. Again, we note for both the linear and the parabolic profiles that the variance increases for data sizes bigger than 2^{15}. That is, the L^1-norm of the variance of reconstructed values from individual data blocks appears to trend very similarly to the true L^2-norm errors, and so we propose using the former as a stand-in for the latter in deciding how to block-divide the data in the present setting. Figure 4.5 thereby confirms that a better result can be both obtained and recognized here when averaging over $B = 8$ or $B = 16$ blocks corresponding to blocks of size 2^{15} or 2^{16}. We remark that there are numerous sources of error in the present reconstruction, including errors in the numerical integration, the numerical convolution, and the minimization itself.

Using the result of the block-averaging technique investigated in the previous three error plots (Figures 4.3, 4.4, and 4.5) we can now reconstruct the velocity profile at five points, $M = 5$, for the linear case with $B = 16$ blocks. In Figure 4.6 we examine both the spread of the values obtained for each block and the average $\overline{\gamma_j}$, $j = 1, \ldots, M$, and standard deviation (plotted as 90% confidence interval error bars for the block reconstruction values).

Finally, we apply the block-averaging technique on the parabolic (Figure 4.7(a)) and exponentially decaying (Figure 4.7(b)) test velocity profiles at $M = 5$ points and $B = 16$ blocks. During our proof-of-principle calculations, we sometimes encountered

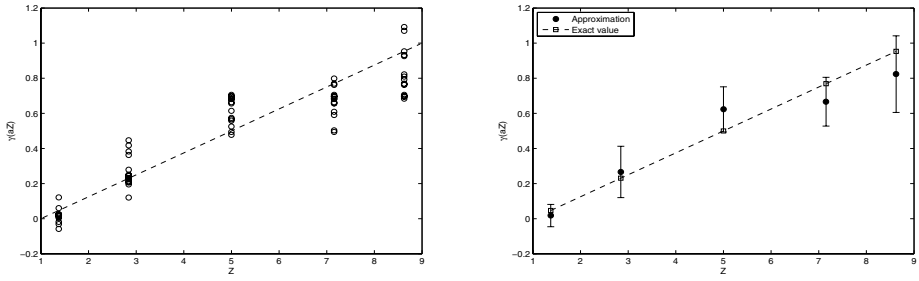

(a) Scatter plot (b) Errorbar plot

FIG. 4.6. *Scatter plot of the different block reconstructed values* γ_j^k, $j = 1, \ldots, M$, $k = 1, \ldots, 16$, *and block-averaged* $\overline{\gamma_j}$, $j = 1, \ldots, M$, *with* 90% *confidence interval for the linear test profile with* $B = 16$ *and* $M = 5$.

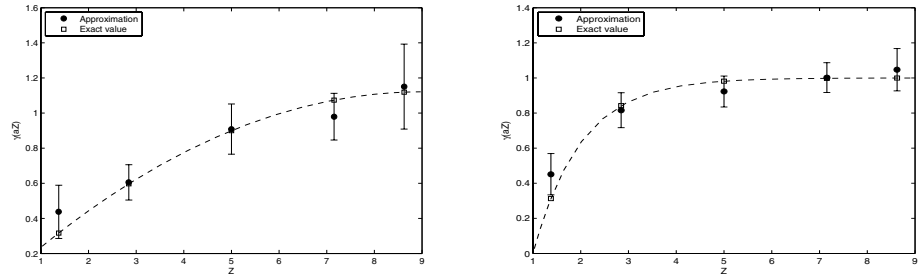

(a) Parabolic profile (b) Exponentially decaying profile

FIG. 4.7. *Errorbar reconstruction for the parabolic and exponentially decaying profile with* $B = 16$, $M = 5$, *and* 90% *confidence interval.*

data sets for which the reconstruction performed particularly poorly, as evidenced by clear jumps in the reconstructed values as might suggest discontinuous velocity profiles. Such poorly performing data was a simple consequence of the state of the random number generator in the simulations; presumably similarly quirky experimental data is not wholly uncommon, and so such reconstructions must therefore, of course, always be questioned, particularly if they indicate highly unlikely results. Finally, we additionally remark that the near-wall region velocity profile is usually assumed to be linear or parabolic, and the exponential case is experimentally unlikely for the present purposes except when the imaged region is large compared to the scale of electroosmotic layers.

To conclude this section we plot the averaged reconstructed mean $\overline{\gamma_j}$, $j = 1, \ldots, M$ (full symbols), compared to their true values (open symbols) at three ($M = 3$) and seven ($M = 7$) points for both the linear (square) and the parabolic (circle) test profiles together in the same figure (Figure 4.8). Figures 4.7 and 4.8 clearly demonstrate that we are able to statistically reconstruct the main behaviors of and distinguish between different profiles (linear, parabolic, and exponentially decaying test profiles) using multiple collocation points ($M = 3, 5, 7$) across the measured region.

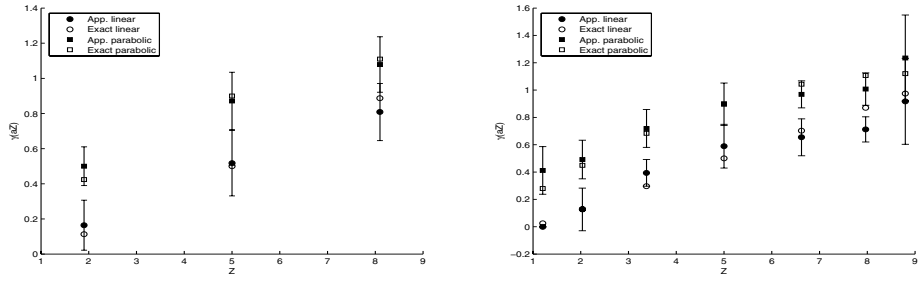

(a) $M = 3$ (b) $M = 7$

FIG. 4.8. *Block-averaged reconstruction ($B = 16$) at $M = 3$ and $M = 7$ points for the linear (square) and parabolic (circle) test profiles (full symbols) together with their respective exact values (empty symbols), with* 90% *confidence intervals on the reconstructed values.*

5. Reconstruction with cross-correlated velocities. In the previous section we used perfect mean displacements between two image windows. In this section, first we describe the idea behind PIV approximate mean measurements and then how they influence the reconstruction algorithm.

PIV is an illumination technique combined with image processing to obtain components of the mean velocity by measuring the mean displacement over a lag time. At microscales, the sample is illuminated with laser sheets and cross-correlation techniques (see [15], [11], [10]) producing a three-dimensional velocity profile. In nano-PIV (nPIV), total internal reflection fluorescence microscopy is used to image tracer particles [12], [14]. When light undergoes total internal reflection for angle of incidence larger than the critical angle, an evanescent wave is created and propagates parallel to the interface with an exponentially decaying intensity. Zettner and Yoda [16] report errors in the approximation of the mean of the order of 10%, while Sadr, Li, and Yoda [13] estimate that nPIV leads to an error of about 6% in the approximation of the mean x-displacement. We remark that for the well-established technique of μPIV, Meinhart, Wereley, and Santiago [11] conclude that the ensemble-averaged displacements lie within 2% of their true values.

The parameters in our computer simulations are chosen to closely match experimental parameters [12]: the sizes of the region of interest are $\delta x = 25\,\mu$m, $\delta y = 5\,\mu$m, and $\delta z = 450\,$nm, the radius of a particle is $a = 50\,$nm, and the number of particles is 64. We note that both background image noise and particle drop-in/-out between the two images also degrade the PIV measurement, but we ignore both effects here for simplicity. Therefore the particles are uniformly distributed in the z-direction between two measurements. Once the image matrix is generated, the approximate x- and y-displacement over a window is determined using cross-correlation [15], [11], [10]. The cross-correlation function is the two-dimensional discrete convolution of two image matrices. The location of the maximum peak of the cross-correlation function gives the mean x- and y-displacement between two windows. To gain subpixel accuracy, a Gaussian surface fitting algorithm with 8 to 11 neighbors is typically used.

Because the previously described technique requires significant experimental agility in the choice of the size of the window over which the displacements are obtained and in the ratio of overlapping of the windows, a threshold criteria for eliminating bad displacement vectors has to be adopted (see [7]). Instead of using a computer

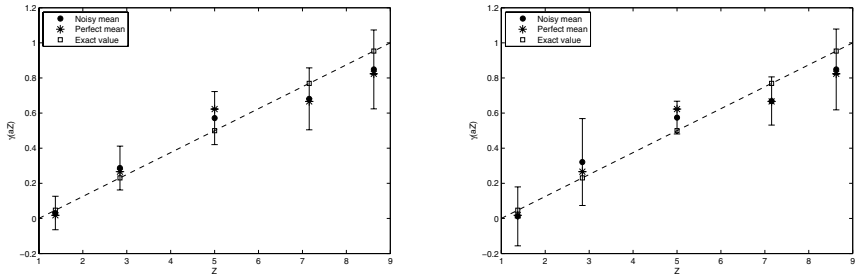

(a) PIV data with 5% relative error (b) PIV data with 10% relative error

FIG. 5.1. *Reconstruction with* 5% *and* 10% *approximated PIV means averaged over* $B = 16$ *blocks and compared with reconstruction from perfect means for the linear case.*

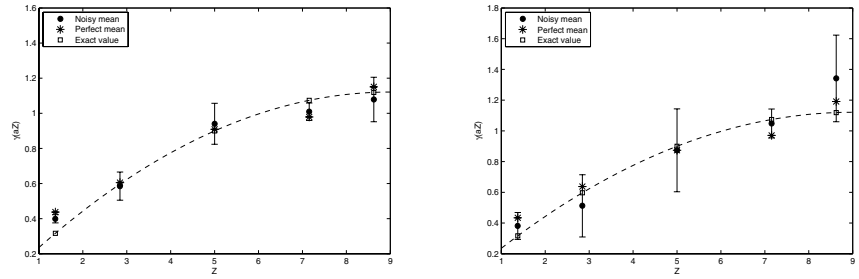

(a) PIV data with 5% relative error (b) PIV data with 10% relative error

FIG. 5.2. *Reconstruction with* 5% *and* 10% *approximated PIV means averaged over* $B = 16$ *blocks and compared with reconstruction from perfect means for the parabolic case.*

analogue to PIV techniques with a threshold which will lead to the generation of more data, here we mimic the effect of these additional experimental errors by adding normally distributed relative errors with standard deviations of 5% and 10% with respect to the overall mean of the perfect mean displacements from our simulations. Then we apply the statistical reconstruction algorithm at $M = 5$ with averaging over $B = 16$ blocks on those two distinct noisy data sets to obtain the results of Figure 5.1 for the linear case and Figure 5.2 for the parabolic test profile. The increasing spread in the extent of the confidence intervals with increasing measurement error demonstrated in Figures 5.1 and 5.2 shows that, while error in the measurement of the mean x-displacement on the scale of that described in the PIV literature definitely affects the reconstructed results and confidence intervals, even at 10% relative errors the reconstructed values are promising. Moreover, if experimental uncertainties can be reduced to about 5%, as pursued in the literature [12], [14], then the block-averaging statistical reconstruction here appears to perform essential as well as with perfectly measured displacements, as illustrated in both Figures 5.1(a) and 5.2(a). We remark that the approximation at the last point Z_M is the worst. This might be caused by some numerical artifacts imposed by the artificial upper wall elastic boundary condition, but we have not been able to pinpoint it precisely so far. However, since the goal is to obtain a better approximation of the velocity profile in the very near-wall region, this is not a major drawback.

6. Discussion. We have successfully demonstrated that it is possible to use the correlation between unknown velocity profiles $\gamma(aZ)$ and known wall-hindered diffusion coefficient $D(z)$ to reconstruct the velocity values with reasonable precision at multiple collocation points within the depth of an imaged window, reconstructing the out-of-plane z-dependence using only measured in-plane displacements, with examples from three basic test flows (linear, parabolic, and exponentially decaying).

We emphasize that all previously reported experimental values, except the recently developed multilayer nPIV (see [9]), obtain a single value for the velocity over the entire region of observation, namely the mean located in the center of the field of focus. The present reconstruction algorithm, approximating the behavior of the deterministic velocity at M (typically $M = 3, 5, 7$) points scattered over the imaged region, is thus a significant improvement.

The reconstruction uses block averaging, and the error plots have demonstrated that it is better to approximate the profile individually over data set blocks of size 2^{14} and to average the result over 8 or 16 consecutive blocks than processing all of our simulated data at once. Importantly, this is computationally fast: the mimimum of the likelihood function ϕ in (4.7) is found in less than 30 minutes on a desktop machine. In contrast, each Milstein-scheme simulation used to generate data here required on the order of 10 days on the same processor. This reconstruction does not use any information about the intensity function and offers an alternative approach to the recently developed multilayer PIV techniques [6], [9] which attempt to infer distance from the wall from image intensities. An interesting direction for future development is the possibility of combining the imperfect (from polydispersity) out-of-plane intensity information with the present statistical method.

The amount of data used in the reconstruction process may seem staggering, but a comparison with data actually captured in experiments indicates that such data sets can be achieved in a reasonable time. For example, Guasto, Huang, and Breuer [4] track over 140000 single quantum dots from 900 image pairs to obtain a single approximation over the entire region. Li, Sadr, and Yoda [9] cite a framing rate of about 26Hz leading to a sequence of 100 frames of about 30 particles recorded within 5 seconds. Keeping the same interframe ratio, it will take between 20 minutes and 4 hours to obtain the necessary 2^{18} frames. Moreover, Li et al. report using in their computer simulated multilayer nPIV 2000 frames with 120 particles and 3 windows for each one of their three layers. In other words they use, after having thrown away an unquantified amount of bad data, about 2^{14} mean displacements for 2^7 particles.

The present demonstration assumes that the particles are uniformly distributed between two measurements; once the computational and observation domain are no longer the same, the uniform distribution assumption will be broken due to particle drop-in and drop-out from the window between two measurements. Provided that this distribution can be computed a priori [13], the reconstruction is simply modified to include the nonuniform probability density function of matched particles. The present results are, of course, only a computer-simulated proof of concept, and more physical effects need to be included for proper use on experimental data, perhaps including the effects of background noise in the images, particle polydispersity, and particles dropping in and out of the field of vision.

Acknowledgments. The authors would like to thank Minami Yoda, Haifeng Li, and Reza Sadr in the Woodruff School of Mechanical Engineering at the Georgia Institute of Technology for providing the experimental problem and for fruitful discussions.

REFERENCES

[1] M. A. Bevan and D. C. Prieve, *Hindered diffusion of colloidal particles very near to a wall: Revisited*, J. Chem. Phys., 113 (2000), pp. 1228–1236.

[2] D. L. Ermak and J. A. McCammon, *Brownian dynamics with hydrodynamic interaction*, J. Chem. Phys., 69 (1978), pp. 1352–1360.

[3] G. G. Fuller, J. M. Rallison, R. L. Schmidt, and L. G. Leal, *The measurement of velocity gradients in laminar flow by homodyne light-scattering spectroscopy*, J. Fluid Mech., 100 (1980), pp. 555–575.

[4] J. S. Guasto, P. Huang, and K. S. Breuer, *Statistical particle tracking velocimetry using molecular and quantum dot tracer particles*, Exp. Fluids, 41 (2006), pp. 869–880.

[5] D. J. Higham, *An algorithmic introduction to numerical simulation of stochastic differential equations*, SIAM Rev., 43 (2001), pp. 525–546.

[6] P. Huang, J. S. Guasto, and K. S. Breuer, *Direct measurement of slip velocities using three-dimensional total internal reflection velocimetry*, J. Fluid Mech., 566 (2006), pp. 447–464.

[7] S. Jin, P. Huang, J. Park, J. Y. Yoo, and K. S. Breuer, *Near-surface velocimetry using evanescent wave illumination*, Exp. Fluids, 37 (2004), pp. 825–833.

[8] P. E. Kloeden and E. Platen, *Numerical Solution of Stochastic Differential Equations*, Springer-Verlag, Berlin, 1999.

[9] H. Li, R. Sadr, and M. Yoda, *Multilayer nano-particle image velocimetry*, Exp. Fluids, 41 (2006), pp 185–194.

[10] D. F. Liang, C. B. Jiang, and Y. L. Li, *A combination correlation-based interrogation and tracking algorithm for digital PIV evaluation*, Exp. Fluids, 33 (2002), pp. 684–695.

[11] C. D. Meinhart, S. T. Wereley, and J. G. Santiago, *PIV measurements of a microchannel flow*, Exp. Fluids, 27 (1999), pp. 414–419.

[12] R. Sadr, H. Li, and M. Yoda, *Impact of hindered Brownian diffusion on the accuracy of nano-particle image velocimetry data*, Exp. Fluids, 38 (2004), pp. 90–98.

[13] R. Sadr, H. Li, and M. Yoda, *Bias due to hindered Brownian diffusion in near-wall velocimetry*, in Proceedings of the 6th International Symposium on Particle Image Velocimetry, 2005.

[14] R. Sadr, M. Yoda, Z. Zheng, and A. T. Conlisk, *An experimental study of electro-osmotic flow in rectangular microchannels*, J. Fluid Mech., 506 (2004), pp. 357–367.

[15] S. T. Wereley and C. D. Meinhart, *Micron-resolution particle image velocimetry*, in Diagnostic Techniques for Microfluidics, K. Breuer, ed., Springer-Verlag, Berlin, 2005, pp. 51–110.

[16] C. Zettner and M. Yoda, *Particle velocity field measurements in a near-wall flow using evanescent wave illumination*, Exp. Fluids, 34 (2003), pp. 115–121.